Supplementary Information for

Microwatt 3D printing metal nanostructures by photothermally-activated Coulombic potential

Xianzhi Zeng[1], Jinping Su[1], Hongbing Zhu[2], Shichao Song[1], Xiangping Li[1]*, Yaoyu Cao[1]*, Min Gu[3,4]*

[1]Institute of Photonic Technology, College of Physics and Optoelectronic Engineering, Jinan University; Guangzhou, Guangdong 510632, China.

[2]Institute of New Energy Technology, College of Physics and Optoelectronic Engineering, Jinan University; Guangzhou, Guangdong 510632, China.

[3]School of Artificial Intelligence Science and Technology, University of Shanghai for Science and Technology; Shanghai 20093, China.

[4]Institute of Photonic Chips, University of Shanghai for Science and Technology; Shanghai 20093, China.

Corresponding authors: Xiangping Li, xiangpingli@jnu.edu.cn; Yaoyu Cao, yaoyucao@jnu.edu.cn; Min Gu, gumin@usst.edu.cn;

Contents

Supplementary Note 1 | Optical diffraction limit in TPLP

Throughout the context, optical diffraction limit is evaluated by the full width of the ideal laser focus. In particular, calculation of focal intensity distribution $I_{focus}(x,y,z)$ is achieved by evaluating the vectorial Debye integral[44]

$$\mathbf{E}_{focus}(x,y,z) = \frac{i\lambda_0 f}{4\pi^2 \varepsilon_r^{(ink)}} \mathrm{FT}\left\{ \frac{\mathbf{E}_{pupil}(\theta,\varphi)}{\cos\theta} e^{ik_z z} \right\}$$

$$I_{focus}(x,y,z) = \mathbf{E}_{focus} \cdot \mathbf{E}_{focus}^{*}$$

in terms of Fourier transform of the electric field at the pupil plane $\mathbf{E}_{pupil}$, assuming that the monochromatic laser with free-space wavelength λ_0 is tightly focused by an objective with focal length f into a homogeneous immersion medium with relative permittivity $\varepsilon_r^{(ink)}$. Numerical implementation is achieved using chirped-z transform algorithm for efficient evaluation of the discretized 3D focal field. For typical optical setup used in this work, the values of optical diffraction limit are calculated and summarized in Supplementary Table S2.

In practice, to avoid undesired scattering by the as-printed parts, invert configuration is adapted and the laser beam is focused through the thick electrolyte solution (measured to be ~100 μm for the sample configuration used in Methods) during printing (Fig. S2). Both the near-UV laser wavelength (405 nm) and in-depth focusing impose difficulties on complete aberration compensation for the present experimental condition, because of the large refractive index mismatch with the coverslip. Experimentally, the lateral full widths of the focus were measured to be about 420 nm and 430 nm along the X and Y axes, respectively. In spite of the approximately 30% broadenings, the measured values well match the simulations in which the influences of aberrations are taken into account (Fig. S3).

For the axial dimension, stretching of the laser focus along the optical axis is also observed, leading to degraded axial resolution. In this work, the typical axial feature size is measured to be ~630 nm (Fig. 4g).

Supplementary Note 2 | Laser-induced optical and thermal effects of nanometals

The optical properties of metals dictate both the lossy nature and surface plasmon resonances of metal nanoparticles (NPs) in ultraviolet to visible range. Particularly, excitation of surface plasmons (SPs) near the resonant frequency ω and the following decay of SPs are the physical sources of electromagnetic (EM) field concentration and the parasitic photothermal heating in TPLP[6,7].

1. Method for plasmonic effect simulations

In this work, boundary element method (BEM) is employed for fast calculation of plasmonic effects of the photoreduced NPs. In brief, (electric) scalar potential ϕ and (magnetic) vector potential $\mathbf{A}$ at arbitrary field point $\mathbf{r}$ are evaluated by[45,46]:

$$\begin{aligned}\phi(\mathbf{r}) &= \phi_{inc}(\mathbf{r}) + \oint G(\mathbf{r},\mathbf{s})\sigma(\mathbf{s})\,da \\ \mathbf{A}(\mathbf{r}) &= \mathbf{A}_{inc}(\mathbf{r}) + \oint G(\mathbf{r},\mathbf{s})\mathbf{h}(\mathbf{s})\,da\end{aligned}, \tag{S1}$$

where ϕ_{inc} and $\mathbf{A}_{inc}$ denote the potential perturbations imposed by the incident wave. The terms $\sigma(\mathbf{s})$ and $\mathbf{h}(\mathbf{s})$ are the so-called auxiliary surface charge and surface current at boundary surface point $\mathbf{s}$, respectively, and $G(\mathbf{r},\mathbf{s})$ is the dyadic Green's function. The induced (scattered) fields can be computed through the relations:

$$\begin{aligned}\mathbf{E}_{sca}(\mathbf{r}) &= ik\mathbf{A}(\mathbf{r}) - \nabla\phi(\mathbf{r}) \\ \mathbf{H}_{sca}(\mathbf{r}) &= \nabla\times\mathbf{A}(\mathbf{r})\end{aligned}, \tag{S2}$$

in which k is the wavenumber in the dielectric medium. Subsequently, the absorption and scattering cross sections, σ_{abs} and σ_{sca}, of the metal NPs can be determined simply by evaluating the normalized power flow P through an imaginary surface enclosing the NPs[47]:

$$\begin{aligned}\sigma_{abs} &= \frac{P_{abs}}{|\mathbf{S}_{inc}|} = \frac{-\oint \mathbf{S}_{tot}\,da}{|\mathbf{E}_{inc}\times\mathbf{H}_{inc}^{*}|} \\ \sigma_{sca} &= \frac{P_{sca}}{|\mathbf{S}_{inc}|} = \frac{\oint \mathbf{S}_{sca}\,da}{|\mathbf{E}_{inc}\times\mathbf{H}_{inc}^{*}|}\end{aligned}, \tag{S3}$$

where $\mathbf{S}$ is the time-averaged Poynting vector corresponding to the incident ($\mathbf{S}_{inc}$), scattered ($\mathbf{S}_{sca}$), or the total field ($\mathbf{S}_{tot}$).

2. SP enhanced photothermal heating

(a) Calculation of steady-state temperature distribution

Under continuous-wave illumination, the heat-dissipation power Q of a source NP can be calculated with the knowledge of absorption cross section at frequency ω:

$$Q \approx Q(\mathbf{r}_s) = \sigma_{abs}(\omega) I(\mathbf{r}_s, \omega), \tag{S4}$$

where $I(\mathbf{r}_s)$ is the intensity at the position $\mathbf{r}_s$ that the source NP locates. In steady state, the resulting temperature distribution due to the local heat source is governed by the heat equation:

$$-\nabla\left[\kappa \nabla T(\mathbf{r})\right] = \nabla Q(\mathbf{r}), \tag{S5}$$

with κ be the thermal conductivity of the media.

To solve Eq. (S5) for the experimental configuration, where complex source structures along with stratified media might be involved, the thermal Green's function method discussed by Baffou et.al is used[29]. In brief, an arbitrary metal structure is first volumetrically meshed into N_{cell} cubic cells, to each of which an imaginary heat source is allocated. For source NP in ink solution, which is separated from the substrate by single, flat interface, the thermal Green's function $G(\mathbf{r})$ can be determined, using the method of image, to be:

$$G(\mathbf{r}, \mathbf{r}_i) = \frac{1}{4\pi\kappa^{(ink)}} \frac{1}{|\mathbf{r} - \mathbf{r}_i|} \tag{S6}$$

for printing in bulk solution with thermal conductivity $\kappa^{(ink)}$, and

$$G(\mathbf{r}, \mathbf{r}_i) = \frac{1}{4\pi\kappa_1} \left(\frac{1}{|\mathbf{r} - \mathbf{r}_i|} - \frac{\kappa^{(sub)} - \kappa^{(ink)}}{\kappa^{(sub)} + \kappa^{(ink)}} \frac{1}{|\mathbf{r} - \mathbf{r}_i^*|} \right) \tag{S7}$$

for printing near the substrate with thermal conductivity $\kappa^{(sub)}$. While $\mathbf{r}_i$ denotes the position vector of the ith imaginary source, $\mathbf{r}_i^*$ is the position vector the of the image of the ith source in the substrate. Next, the inner temperature rise ΔT_0 is retrieved, by energy conservation and prescribed boundary conditions, with the help of an imaginary metal nanosphere that is assumed to share identical heat dissipation power as the structure of interest. Precisely, ΔT_0 is obtained by:

$$\Delta T_0 = \frac{Q}{4\pi\kappa^{(ink)} R_{eff}}. \tag{S8}$$

The radii R_{eff} of the imaginary metal nanosphere can be computed by:

$$r_0^{eff} = \sum_{i=1}^{N_{cell}} \sum_{j=1}^{N_{cell}} \left(L^{-1}\right)_{ij}. \tag{S9}$$

The L matrix is determined simply based on the position vectors of the physical sources $\mathbf{r}_i$ and the image sources $\mathbf{r}_i^*$. The matrix elements L_{ij} reads:

$$L_{ij} = \frac{1}{\left|\mathbf{r}_i - \mathbf{r}_j\right|} \tag{S10}$$

for in-solution printing and

$$L_{ij} = \frac{1}{\left|\mathbf{r}_i - \mathbf{r}_j\right|} - \frac{\kappa^{(sub)} - \kappa^{(ink)}}{\kappa^{(sub)} + \kappa^{(ink)}} \frac{1}{\left|\mathbf{r}_i - \mathbf{r}_j^*\right|} \tag{S11}$$

for near-interface printing with $i \neq j$, otherwise L_{ij} equals the inverse of half spatial sampling step dr. Using Eq. (S6) to Eq. (S11), the temperature distribution in exterior of the source structure can be calculated through:

$$\Delta T\left(\mathbf{r}\right) = \sum_{i=1}^{N} \left[G\left(\mathbf{r}, \mathbf{r}_i\right) \sum_{j=1}^{N} \left(L^{-1}\right)_{ij} \Delta T_0 \right]. \tag{S12}$$

Since the absorption cross sections of the source particles (on the order of 10^4 nm^2) are two order-of-magnitude larger than that of the feed NPs (on the order of 10^2 nm^2, see Fig. S4), the contributions of heat dissipation by the feed NPs to total temperature distribution can be neglected unless the feed NP population reaches 10^3 scale in the focus (Fig. S6). Therefore, for the sake of simplicity, during temperature field calculations, only contributions from the source NPs are included. Also, it should be pointed out that the presence of a metallic feed NP at field point $\mathbf{r}$ leads to equalized temperature gradient for field points nearby. Specifically, from continuity requirement for the heat flux through the NP-ink interface one can easily find that the local temperature gradient suffices:

$$\left|\nabla T\right|_{\left|\mathbf{r}-\mathbf{r}_f\right|=R_f} \approx \frac{3\kappa^{(ink)}}{2\kappa^{(ink)} + \kappa^{(Ag)}} \left|\nabla T\left(\mathbf{r}_f\right)\right|,$$

where $\mathbf{r}_f$ represent the position vector directed from the focus to the mass center of the feed NP

and R_f is the hydrodynamic radius of the feed NP. Because of the high thermal conductivity of silver (429 W/m·K), 'flattened' temperature gradient is expected near the surface of the feed NPs. As would be discussed in Supplementary Note S3.2, this property gives rise to suppressed osmotic diffusions of the feed NPs in our case.

(b) Validation of steady-state analysis for TPLP

One the one hand, from Eq. (1) in the main text (and Eq. (S35) below) the effectiveness of NP confinement in TPLP is dictated by the focal temperature gradient. Numerical simulations reveal that with the presence of single dominating source NP in the focus (Figs. S4 and S7), the maximum focal temperature gradient value is on the scale of 1 K/nm. Approximately, a gradient value variation over 0.1 K/nm can be regarded significant to induce 'considerable' change on the CC field thereby the NP transport behaviors. The corresponding change in feature size of the NP structure is derived to be ~1 nm, based on calculations of feature-size dependent focal temperature gradient for a source NP in the laser focus (Fig. S7). Accordingly, the characteristic growth time τ_{grow} for inducing such 'noticeable' size change is estimated to be of 1-ms scale through evaluating the first-order derivative of the exposure-time dependent feature size curve shown in Fig. 2n.

On the other hand, the characteristic time τ for the typical system considered in TPLP to reach thermal equilibrium is calculated to be of 1-μs scale, by solving time-dependent heat equation:

$$\rho_m c_p \frac{\partial}{\partial t} T(\mathbf{r},t) - \nabla\left[\kappa \nabla T(\mathbf{r},t)\right] = \nabla Q(\mathbf{r},t), \tag{S13}$$

where ρ_m and c_p are the mass density and specific heat capacity. Since τ appears to be three order-of-magnitude smaller than τ_{grow}, the change on focal temperature gradient distribution is considered to be negligible for $(i-1)\tau_{grow} \le t \le i\tau_{grow}$, with $i = 1, 2, 3\cdots$. The validity of steady-state analysis is thus held within one τ_{grow} interval. For the sake of clarity and simplicity, the discussions are restricted within one τ_{grow} interval throughout this work.

3. SP-assisted photoreduction

In TPLP, excitation of SPs of the metal NPs modifies the local (photonic) density of states and

varies spontaneous transition rates of the dipole-like precursor ions. Herein, a semi-classical model is employed to describe the coupling between the plasmonic NPs and the precursor ions[46].

Assuming that the quantum yield of photoreduction (from metal ions to zero-valence atoms) following dipolar excitation is unity, the photoreduction rate is equivalently evaluated by the change on light absorption rate by the metal ions. Specifically, a two-level electric dipole with transition energy $\hbar\omega$ of 3.06 eV (equivalent to a transition wavelength of 405 nm) and dipole moment $\mathbf{p}$ (direction of which is averaged along the three main axes of Cartesian coordinate system) is assumed. The absorption rate of the dipole can be computed using[48]:

$$\frac{\Gamma^{(abs)}}{\Gamma_0^{(abs)}} = \frac{6\pi\varepsilon^{(ink)}}{|\mathbf{p}|^2}\frac{1}{k^3}\mathrm{Im}\left\{\mathbf{p}^* \cdot \mathbf{E}_{sca}\right\}, \tag{S14}$$

where $\varepsilon^{(ink)}$ represents the electric permittivity of the ink solution at frequency ω and $\Gamma_0^{(abs)}$ is the free-space absorption rate. For an ideal two-level system, $\Gamma_0^{(abs)}$ equals

$$\Gamma_0^{(abs)} = \Gamma_0^{(rad)} = \frac{|\mathbf{p}|^2 k^3}{6\pi\varepsilon^{(ink)}}. \tag{S15}$$

Numerical evaluation of Eq. (S18) is achieved by sequentially placing the probe dipole at field points of interest, the transition rate of which is then recorded and normalized to $\Gamma_0^{(abs)}$.

4. <u>SP-induced capping agent desorption</u>

As has been shown in previous reports, photoinduced hot carriers are capable of triggering capping agent desorption from the NP surfaces[49,50]. Considering the intense near-field enhancement (Fig. S10) and efficient hot carrier generation by SP damping in noble metals[7,49], desorption of capping agents (in our case the surfactant ion ND-Sar) from the feed NP surface could be induced as source-feed gap distance is small enough to excite the gap plasmon resonance.

Supplementary Note 3 | Thermal transport of the photoreduced NPs

Based on the experimentally measured feature size range (Fig. 2), the maximum focal temperature rise is calculated to remain mild, with $\Delta T < 80\text{K}$ (Figs. S4-S7). Consequently, for the present configurations thermal convection induced NP transport effects are neglected. The non-equilibrium thermal transports of the elemental feed NPs are ascribed to three mechanisms for TPLP: 1) randomizing Brownian motions, 2) thermo-osmosis driven by electric-double layer force, and 3) Coulombically-confinement (CC) driven by thermoelectricity.

1. Randomizing Brownian motion:

In the TPLP ink, the random collisions between the solvent molecules and the feed NPs give rise to Brownian motion, which fundamentally persists for finite temperature values. Classically, the equation of motion of an unconstrained feed NP with hydrodynamic radius R_f can be described by the Langevin equation[36]:

$$m\frac{d^2\mathbf{r}}{dt^2}+\gamma\frac{d\mathbf{r}}{dt}=\sqrt{2k_BT\gamma}\boldsymbol{\xi}(t), \tag{S16}$$

where m is the mass of the feed NP and $\gamma = 6\pi\eta R_f$ is the Stokes friction coefficient with η the viscosity of the ink solution. The term $\sqrt{2k_BT\gamma}\boldsymbol{\xi}(t)$ on the right-hand side of Eq. (S16) is the Brownian force arising from random collisions, with $\boldsymbol{\xi}$ the random Gaussian vector. Solving Eq. (S16) in overdamping limit leads to an estimation on the mean squared displacement from the release point (set as origin for all simulations) for a time duration Δt:

$$\frac{1}{2}\langle\mathbf{r}\cdot\mathbf{r}\rangle=\frac{k_BT}{\gamma}\Delta t \tag{S17},$$

where the term k_BT/γ is known as the mass diffusion coefficient D_m, i.e.,

$$D_m=\frac{k_BT}{\gamma}. \tag{S18}$$

Using Eq. (S17), a rough estimation shows: for a 10-nm feed NP, released free to move in a heat bath at 323 K (equivalently, $\Delta T = 25\text{K}$) at $t = 0$, the average displacement $\langle\mathbf{r}\cdot\mathbf{r}\rangle^{1/2}$ becomes comparable to the optical diffraction limit (on the order of 100 nm) at times ca. 1 ms from the release. Comparable with typical unit exposure times in common 3D metal laser nanoprinting techniques (on the order of 1 to 10 ms), Brownian motion of the elemental feed NPs cannot be

ignored (Fig. 2e).

In the presence of a harmonic confining potential well, Eq. (S16) becomes:

$$m\frac{\partial^2 \mathbf{r}}{\partial t^2}+\gamma\frac{\partial \mathbf{r}}{\partial t}-\boldsymbol{\chi}\mathbf{r}=\sqrt{2k_BT\gamma}\boldsymbol{\xi}(t), \tag{S19}$$

where $\boldsymbol{\chi}$ is the stiffness of the potential well and connects with the potential energy ΔU via $\chi_i=\nabla_i^2(\Delta U), i=x,y,z$. Since the characteristic timescale for 'noticeable' system change in TPLP is on the order of 1 ms, which is 10 order-of-magnitude larger than the momentum relaxation time (of 10 ps scale) of the feed NPs, the second-order inertia term in Eq. (S18) is neglected during numerical evaluations. Thusly, Eq (18) can be rewritten as:

$$\gamma\frac{\partial \mathbf{r}}{\partial t}-k_r\mathbf{r}=\sqrt{2k_BT\gamma}\boldsymbol{\xi}(t).$$

Using finite difference method, the position vector of the feed NP $\mathbf{r}_m$ at the mth time step can be obtained:

$$\mathbf{r}_m=\mathbf{r}_{m-1}-\frac{1}{\gamma}\boldsymbol{\chi}\cdot\mathbf{r}_{m-1}\Delta t+\sqrt{2D_m\Delta t}\boldsymbol{\xi}. \tag{S20}$$

Eq. (S19) is employed for numerical simulations on the motion trajectories of feed NPs with the presence or absence of the CC potential field (during which both the magnitude and distribution of the focal temperature is fixed). Also, from Eq. (S19) it is straightforward that the existence of a confining potential well (which is 'concave' with positive χ_i) would lead to decreased mean displacement of the feed NPs during each time step and thus suppressed random NP diffusions.

2. <u>Electric double layer driven thermo-osmosis:</u>

In electrolyte solutions, a charged colloid could also electrostatically interact with the mobile ions thereof. In thermal equilibrium, a double-layer structure known as the electric double layer (EDL) is formed screening the colloid[40]. The distance over which the colloid is effectively screened can be characterized by the Debye screening length λ_D. Assuming that each ions species carries Z_i elemental charge e and has a bulk number density of $n_{0,i}$, λ_D reads:

$$\lambda_D=\left(4\pi\lambda_B\sum\nolimits_i^N Z_i^2 n_{i,0}\right)^{-1/2}, \tag{S21}$$

where $\lambda_B=e^2/\left(4\pi\varepsilon_\infty^{(ink)}k_BT\right)$ is the Bjerrum length (~0.6 nm) with $\varepsilon_\infty^{(ink)}$ the static electric

permittivity of the electrolyte ink and k_B the Boltzmann constant.

With finite temperature gradient values, the change of electric potential energy in the EDL causes slip flows tangent to the NP surface[33]. In the spirit of boundary-layer approximation, the consequent NP drift velocity $\mathbf{u}$ can be expressed as the integral of force density $\mathbf{f}$ exerted on the NP subtracted by the gradient of osmotic pressure ∇P within the boundary layer[36]:

$$\mathbf{u} = \frac{2}{3\eta}\int_0^{L_B} \left(\mathbf{f} - \nabla P\right) r dr , \tag{S22}$$

where L_B the boundary layer thickness. The prefactor 2/3 emerges due to orientation average over the NP surface. Concerning solely the contribution from the temperature gradient, it has been shown that for strong electrolyte solution (the concentrations of the solutes of which are well above 10 mmol/L) $\mathbf{u}$ equals:

$$\mathbf{u} = -\frac{\varepsilon_\infty^{(ink)}\zeta^2}{3\eta}\frac{\nabla T}{T} , \tag{S23}$$

where ζ denotes the surface potential of the NP and connects with the surface charges q_{NP} through[51]:

$$q_{NP} \approx \frac{2er_0^{\,2}}{\lambda_D \lambda_B}\sinh\left(\frac{e\zeta}{2k_B T}\right). \tag{S24}$$

In Eq. (S23), the coefficient term on the right-hand side shows the dimension of m^2/s and is defined as the thermophoretic mobility D_T of the colloid by:

$$D_T^{(EDL)} = \frac{\varepsilon_\infty^{(ink)}\zeta^2}{3\eta T} . \tag{S25}$$

Eq. (S25) holds for charged colloids with radii R ranging from $R \gg \lambda_D$ to $R \sim \lambda_D$, and thus holds for both the charged feed NPs and ions in the TPLP ink[34]. Together with Eq. (S23), thermophobic (i.e., hot-to-cold) migration is expected for the feed NPs and the ions, because of the quadratic dependence of surface potential, the non-negative electric permittivity and viscosity of the host ink solution. Utilizing Eq. (S23), the EDL force exerted on a probe feed NP can be evaluated by

$$\mathbf{F} = 6\pi\eta R_f \mathbf{u} . \tag{S26}$$

The potential energy ΔU can then be equivalently evaluated through the reversible work done by the EDL force by quasi-statically maneuvering the feed NP from $\mathbf{r}$ to infinity merely:

$$\Delta U_{EDL}(\mathbf{r}) = -\int_r^{\infty} \mathbf{F}(\mathbf{r}')\, d\mathbf{r}'. \tag{S27}$$

Due to the aforementioned temperature gradient flattening near the feed NP, the thermo-osmotic potential energy probed by single feed NP is weak with magnitude on the $10^{-3} k_B T$ scale (see Figs. 2a, S12). Thus, EDL-force driven thermo-osmosis is negligible in our case and is obscured by the randomizing Brownian diffusion of the feed NPs (Fig. S8).

Back to Eq. (S25), the quadratic surface potential dependence of the thermophoretic coefficient implies that local charge separation demanded for CC could be achieved by differentiating transport velocities between positive and negative ion species by charge density modulations. Accordingly, surfactant ions are introduced during formulation of the TPLP inks. At concentration above the critical micelle concentration, micellization of the surfactant ions yields micellar ions with large charge numbers (~10) compared with the simple ions (unity for sodium and silver ions). The resulted micellar ions thus share $D_T^{(EDL)}$ (~10^{-10} $m^2/s{\cdot}K$) that is about two-order higher than that of the simple counterions (~10^{-12} $m^2/s{\cdot}K$) and are expected to be more susceptible to thermo-osmosis[39]. Using Eq. (S25), it can be found that the osmotic displacement of the micellar ions at a moderate temperature gradient value of 0.5 K/m is readily comparable with the diffraction limits for a time duration of ca. 2 μs, while both the osmotic displacements of the simple ions and feed NPs are negligible. Besides, because of the high aggregation number (see Supplementary Note S4 below) the hydrodynamic radius of the micellar ions $R_{micelle}$ is estimated to be ~10^1 Å. According to Eqs. (S17) and (S18), the corresponding average displacement of Brownian motion is evaluated to be about 1/3 of the simple ions (which share $R_{counterion}$ on the scale of 10^0 Å). The above comparisons indicate that local electric polarization by thermo-osmosis induced charge separation can be well established for the thermal equilibrium timescale., which lays the basics of CC potential field establishment (quantification of the charge separation process would be discussed in the next section).

3. <u>Thermoelectricity induced Coulombic confinement</u>

To quantify CC effect, explicit form of the induced electrostatic field is derived. Generally, the TPLP inks contain N mobile ion species, each of which carries charge $q_i = eZ_i$ and has a number density of n_i. Allowing the presence of non-zero temperature gradient ∇T and electric

field $\mathbf{E}$ beyond ion density gradient ∇n, the ion flux $\mathbf{J}$ of the i[th] mobile species can be written as:

$$\mathbf{J}_i = -\nabla n_i D_{m,i} - n_i D_{T,i}^{(EDL)} \nabla T + n_i D_{E,i} \mathbf{E}, \tag{S28}$$

where $D_{m,i}$, $D_{T,i}^{(EDL)}$ and $D_{E,i}$ are respectively the mass diffusion coefficient, thermophoresis coefficient, and electrophoretic coefficient of the i[th] species. The electrophoretic coefficient, under first-order approximation, takes the form of

$$D_{E,i} = D_{m,i} \frac{eZ_i}{k_B T}.$$

In steady state, the ion flux vanishes for all species, that is, $\mathbf{J}_i = 0$. From Eq. (S28), one can find that in the absence of external field an induced electric field could still exist due to ion concentration and temperature gradients, as has been demonstrated in recent researches[52,53]. Summing Eq. (S28) over all species and multiplying both sides of the equation with D_i / q_i, we obtain:

$$\sum_i^N \frac{q_i \mathbf{J}_i}{D_{m,i}} = -\sum_i^N q_i \nabla n_i + \sum_i^N \frac{q_i^2 n_i}{k_B T} \mathbf{E} - \sum_i^N q_i n_i \frac{D_{T,i}}{D_{m,i}} \nabla T = 0. \tag{S29}$$

has been used. Assuming that the deviations on the local ion densities are small compared with the bulk values so that $n_i = n_{0,i} + \delta n_i \approx n_{0,i}$, Eq. (S29) can be simplified to be:

$$\nabla \rho - \frac{\varepsilon_\infty^{(ink)}}{\lambda_D^2} \mathbf{E} + \sum_i^N q_i n_{0,i} \frac{D_{T,i}}{D_{m,i}} \nabla T = 0, \tag{S30}$$

where Eq. (S21) has been used. Allowing non-zero charge density gradient, the use of Gauss's law $\varepsilon_\infty^{(ink)} \nabla \cdot \mathbf{E} = \rho$ leads to $\nabla \rho = \nabla \left(\varepsilon_\infty^{(ink)} \nabla \cdot \mathbf{E} \right)$. Neglecting permittivity change due to density variation of the ink solution, Eq. (S30) becomes:

$$\left(\nabla^2 - \frac{1}{\lambda_D^2} \right) \mathbf{E} + S \nabla T = 0, \tag{S31}$$

where S is defined as the thermoelectric (Seebeck) coefficient

$$S \equiv \frac{1}{\varepsilon_\infty^{(ink)}} \sum_i^N q_i n_{0,i} \frac{D_{T,i}}{D_{m,i}}. \tag{S32}$$

The thermoelectric S coefficient reflects both the sign and strength of polarization by ion

separation. It can be seen that the multiplication by the factor of $D_{T,i}/D_{m,i}$ modifies the neutrality condition ($\sum_i^N q_i n_{0,i}=0$) and gives rise to non-zero S coefficient, which leads to a particular solution that links with the focal temperature gradient; meanwhile, the sign of S is explicitly determined by the ion species with high thermophoretic mobility but low mass diffusion mobility, and the larger the quotient difference (which is formally defined as Soret coefficient) between positive and negative ions the larger the magnitude of S would be. Consequently, to effectively induce local electric polarization, the aforementioned surfactant ion (see the previous section) is employed.

From Eqs. (S21) and (S30), for radial symmetric system that frequently involved for in-solution printing in TPLP, the temperature distribution simply follows Eq. (S8). The boundary conditions requires that the induced electric field must vanish for $r\to\infty$ but remains finite for $r=R_s$. Again, with Gauss's law the induced electric field satisfies:

$$\mathbf{E}\left(\mathbf{r}=R_s\hat{\mathbf{r}}\right)=\mathbf{E}_0=\frac{\sigma}{\varepsilon_\infty^{(ink)}}\hat{\mathbf{r}}, \tag{S33}$$

in which $\hat{\mathbf{r}}$ is the unit radial vector. Substituting Eq. (S8) into Eq. (S31) and taking use of the boundary conditions, the thermally-activated electric field, which we phrase as Coulombically-confining (CC) field, is solved to be:

$$\mathbf{E}_{CC}\left(\mathbf{r}\right)=\frac{\sigma}{\varepsilon_\infty^{(ink)}}\frac{\mathbf{R}_s}{r}\exp\left(-\frac{r-R_s}{\lambda_D}\right)+S\nabla T\left(\mathbf{r}\right)\left[1-\exp\left(-\frac{r-R_s}{\lambda_D}\right)\right], \tag{S34}$$

The first and the second terms in the right-hand side of Eq. (S34) account for the screened electric fields established due to the residual surface charges and thermally-induced charges, respectively. Because of the screening effect, for r well larger than λ_D (which is less than 1 nm for the strong electrolyte ink used in this work), the first term quickly vanishes, while the second term converges to $S\nabla T$ and predominates. Therefore, incomplete desorption of the ionic capping agents is considered to have little effect on the overall CC field strength. In the limit of zero surface charge, Eq. (S34) reduces to:

$$\mathbf{E}_{CC}\left(\mathbf{r}\right)=S\nabla T\left(\mathbf{r}\right)\left[1-\exp\left(-\frac{r-r_0}{\lambda_D}\right)\right]. \tag{S35}$$

In accordance with Eq. (S35), it can be seen that the spatial profile of the thermally-activated CC

field is dictated by the temperature gradient distribution ∇T, which have not necessarily to be photoinduced and thusly offers an extra degree of freedom for CC field synthesis by ∇T devising. Besides, since the square bracket part in Eq. (S35) remains positive for $r > R_s$, given fixed ∇T the direction of the CC potential drop is determined by the S coefficient, the sign of which indicates whether positive or negative ions accumulate in the cold region (which in this work is the negative micellar ions). Forced transport of feed NPs towards the hot region can be initiated by charging the feed NPs with same sign as S. As mentioned in the main text, this is achieved by applying a high surfactant concentration that is approx. 4-times of the CMC. Since the adsorption of the surfactant ions on the colloidal nanoparticles is thermodynamically favourable[40], the surfactant ions tend to self-assembly into ionic shell on the feed NP surfaces and high concentration values guarantee sufficient supply of surfactant ions for such chemical charging process.

With Eq. (S25), the CC potential energy probed by a feed NP with charge q_{probe} can be evaluated, in quasi-static manner, via

$$\Delta U_{CC}\left(\mathbf{r}\right) = -\int_{r}^{\infty} q_{probe}\mathbf{E}_{CC}\left(\mathbf{r}'\right)d\mathbf{r}'. \tag{S36}$$

The activation of CC field by single dominating source NP readily leads to effective capturing of surrounding feed NPs (Figs. 2f, 2g, and S9), which can further consolidate the dominance of the source NPs by continual feeding and SP-assisted photochemical joining. We also need to point out that without the central dominating NP(s) the feed NPs alone cannot effectively induce robust CC potential even for a large NP number up to 500 (Fig. S6).

Supplementary Note 4 | Size and charge number of the photoreduced NPs

As reported in previous publications[11,13] and evidenced by Figs. 2h-j, 3c and 3d, the sarcosinate surfactants could serve as growth inhibitor for photoreduced silver nanoparticles (NPs), circumventing over-agglomeration and effectively reducing the grain size of the printed structures. Supportively, a reference experiment is conducted for rough estimation on the average size of the feed NPs. In particular, the near-UV (405 nm) source is replaced with a blue (473 nm) source to ensure sufficient photoreduction efficiency but suppressed absorption by the feed NPs (Fig. S4). Using an objective with numerical aperture lower than that for common TPLP experiments (UPlanFL N 60×/0.90/0.13-0.21), silver microwires consisted of loosely-packed silver NPs are obtained at a exposure condition of 613 μW @ 600 nm/s (power requisite increased due to lowered photosensitivity of the ink and absorption cross section of the NPs at longer wavelength). Feature size statistics of NPs in the microwires shows a near-Gaussian distribution, The expectation value is fitted to be ca. 13 nm with a standard deviation of ~2 nm (Fig. S10). For this reason, the elemental feed NPs, are presumed to be 10-nm spherical NPs throughout the context.

Also, since the typical concentration value of ND-Sar used in this work is well-above the first critical micelle concentration[37], sufficient supply of surfactant ions for feed NP charging is expected. Taking common surface potential values (of 10 mV scale) of silver nanoparticles in electrolyte solutions[54,55], the charge number of the feed NPs is estimated to range between 20~80 using Eq. (S24). Assuming moderate charging of the feed NPs, a charge number of 50 is used for simulations.

Dictated by the length of the hydrophobic tail[37,38], the sarcosinate salt family shares aggregation numbers on the order of 10^1, for which reason the charge number of the micellar ions is chosen to be 10 for all simulations in this work.

Supplementary Note 5 | Exclusion of optical trapping as dominant mechanism

On the one hand, a commercially-available silver NP suspension with optical density (OD) of 2 is employed as the alternative ink for conduction of reference optical trapping test with the same 3D nanoprinter used for TPLP. After 1-min irradiation at laser power up to 660 μW, which is 3-times larger than that used for 3D TPLP experiments, no significant refractive index contrast can be observed, indicating that silver structures cannot be formed by gradient-force directed particle assembly in our case (Fig. S13 and Supplementary Movie S4).

Second, the optical force probed by a 10-nm feed NP within the laser focus is computed using[48]:

$$F_i = \sum_j \int_V \frac{\partial}{\partial x_j} T_{ij} d^3x . \tag{S37}$$

The integration is taken within a sphere enclosing the NP, and T_{ij} is the Maxwell stress tensor that

$$T_{ij} = \varepsilon^{(ink)} \left[E_i E_j + c^2 B_i B_j - \frac{1}{2}\left(\mathbf{E}\cdot\mathbf{E} + c^2 \mathbf{B}\cdot\mathbf{B} \right) \delta_{ij} \right], \tag{S38}$$

where $\mathbf{B}$, c, are the magnetic induction and the speed of light, respectively, and δ_{ij} refers to the Kronecker delta. The optical force computed using Eq. (S37) is found to be weak (on 1fN scale), and the corresponding potential energy ΔU_{OT} is evaluated to be far less than $k_B T$ (Fig. S13).

Putting together, consequently, optical trapping is considered to be insufficient to cause directional migration and assembly of the feed NPs, and optical trapping is excluded as the leading mechanism in TPLP.

Supplementary Note 6 | Nonlinear exposure dose accumulation in TPLP

To semi-quantitatively demonstrate the link between exposure dose accumulation and the potential fields, a simple classical model is introduced.

1. Exponential feed NP redistribution

At thermal equilibrium, the feed NPs share identical temperature with the surroundings through heat conduction, thus the spatial variations in energy are dominated by the potential terms, i.e., the CC potential, thermo-osmotic potential, etc. From Figs. S9, S11 and S12. Applying mean-field approximation, the probability density $p(\mathbf{r})$ for a feed NP to settle at some field point $\mathbf{r}_j$ in the focus, viz., the field point $\mathbf{r}_j$ to be populated by the feed NP, at certain absolute temperature T follows[36]:

$$p(\mathbf{r}_j) = \frac{p_0(\mathbf{r}_j)\exp\left[-\beta\sum_i \Delta U_i(\mathbf{r}_j)\right]}{\int_{focus} p_0(\mathbf{r}')\exp\left[-\beta\sum_i \Delta U_i(\mathbf{r}_j)\right]d\mathbf{r}'}, \tag{S39}$$

where ΔU_i is the potential energy contributed from the ith effect and β the thermodynamic beta that equals $1/(k_B T)$. $p_0(\mathbf{r})$ is the initial weight function that reflects the 'likelihood' of populating the field points through in-situ photoreduction and correlates with the focal intensity distribution to the first order via:

$$p_0(\mathbf{r}_j) = \frac{I(\mathbf{r}_j)}{\int_{focus} I(\mathbf{r}')d\mathbf{r}'}. \tag{S40}$$

From Figs. S9, S11 and S12, $\sum_i \Delta U_i$ becomes negative and monotonically decreased with diminishing source-feed interparticle distance with the presence of CC potential, indicating that confinement of feed NP towards the source NP is energetically preferable and thus leading to concentrated feed NP distribution in TPLP. Also, it should be noted during NP distribution simulations, the volume exclusion effect of the NPs along with short-range interactions (e.g. van der Waals potential, which decays with $1/|\mathbf{r}_s - \mathbf{r}_f|^6$ and thus has little effect unless the interparticle distance is on the scale of Debye length) between the NPs are neglected for the sake of simplicity

2. *Nonlinear feeding in TPLP*

At thermal equilibrium, the number density of the feed $n_f(\mathbf{r})$ can be computed with the help of Eq. (S39) so that:

$$n_f(\mathbf{r}) = Mp(\mathbf{r}). \tag{S41}$$

The total number of feed NPs M generated within one τ_{grow} interval can be roughly estimated through:

$$M = \frac{\int_{focus} \tau_{grow} I(\mathbf{r})\, d\mathbf{r}}{\int_{focus} \tau_{grow} I_{th} d\mathbf{r}}. \tag{S42}$$

I_{th} denotes the intensity threshold, on exceeding which could feed NPs be photochemically generated. In regular experimental configurations discussed in this work, without the presence of CC field n_f roughly follows intensity distribution, i.e., $n_f = n_0 = Mp_0$ (Fig. 2b). However, the establishment of CC field, which leads to a potential energy of $-6k_BT$ (for a feed NP with charge number of 50) at a focal temperature gradient value of ~0.8 K/nm (Fig. S9), modifies the potential energy distribution within the laser focus and reshapes feed NP distribution. According to Eq. (S39), the probability of 'finding' a feed NP in vicinity of the source NP can be increased by a factor of 10 (Figs. 2g, S15). The confining and subsequent joining of feed NPs to the source NP causes additive volume change and thus feature size change of the source structures. In radial symmetric systems, the number of available NPs m for feeding the as-printed source structures at specific radial coordinate r (in one τ_{grow} interval) can be expressed as

$$m(r, I) = n_f(r, I) 4\pi r^2 dr \tag{S43}$$

and satisfies $M = \int_{R_s}^{\infty} m(r)\, dr$. The feature size change ΔD can then be roughly estimated via

$$\Delta D = 2\Delta R_s = m(r, I) \frac{R_f^{\,3}}{3R_s^{\,2}} \tag{S44}$$

The order of intensity dependency of the NP feeding can be evaluated by the logarithmic derivative as follows[5]:

$$slope = \frac{\partial \log(\Delta D)}{\partial \log(I)}. \tag{S45}$$

The nature of nonlinear NP feeding in TPLP is explicitly manifested by the exponentially scaling n_f. Notably, for CC potential field shown in Fig. 2f the nonlinear slope is derived to be about 2.3, which is in sharp contrast to the unity value for the case without CC field (Fig. 2k). Because of the nonuniform feed NP distribution, the nonlinear slope appears to be non-constant in the laser focus. The nonlinearity gradually decreases as the radial coordinate increases. The spatial inhomogeneity indicates that exposure dose accumulation is efficient only in proximity of the source NP surface (Fig. S15), at which both the feed NP density and photoreduction rate are high compared with the focal periphery. This property not only endows enhanced exposure dose confinement within the focus, but also attributes to the cleaner substrates in TPLP experiments compared with the control printing experiment group (since most feed NPs are fed to the source structures, and the growth of the feed NPs themselves are limited due to the inhibitive surfactant shell and the low optical nonlinearity at positions far away from the source structure, see Figs. 2c-f, S14).

Supplementary Fig. S1 | Main chemical composition of TPLP inks

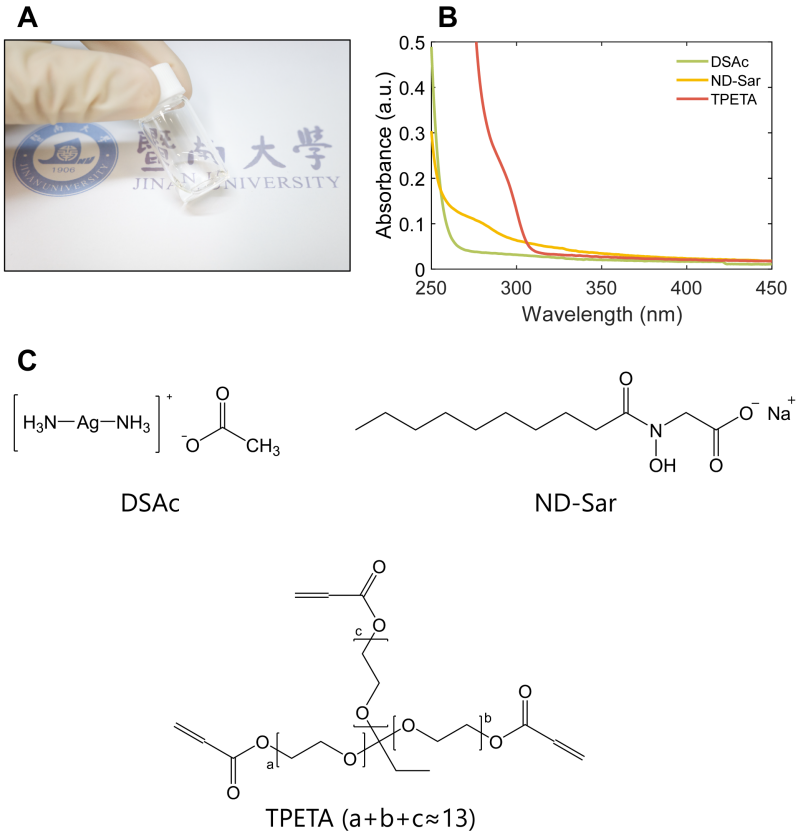

(**A**) Photograph of the as-prepared TPLP ink used in this work. (**B**) UV-Vis absorption spectra of the main ingredients of the ink, the low absorbance at the operation wavelength of TPLP minimizes undesired photoreduction in the bulk solution during in-depth printing. (**C**) Chemical structures of the metal precursor ion, surfactant ion, and the organic reducing agent.

Supplementary Fig. S2 | Optical system and sample configurations

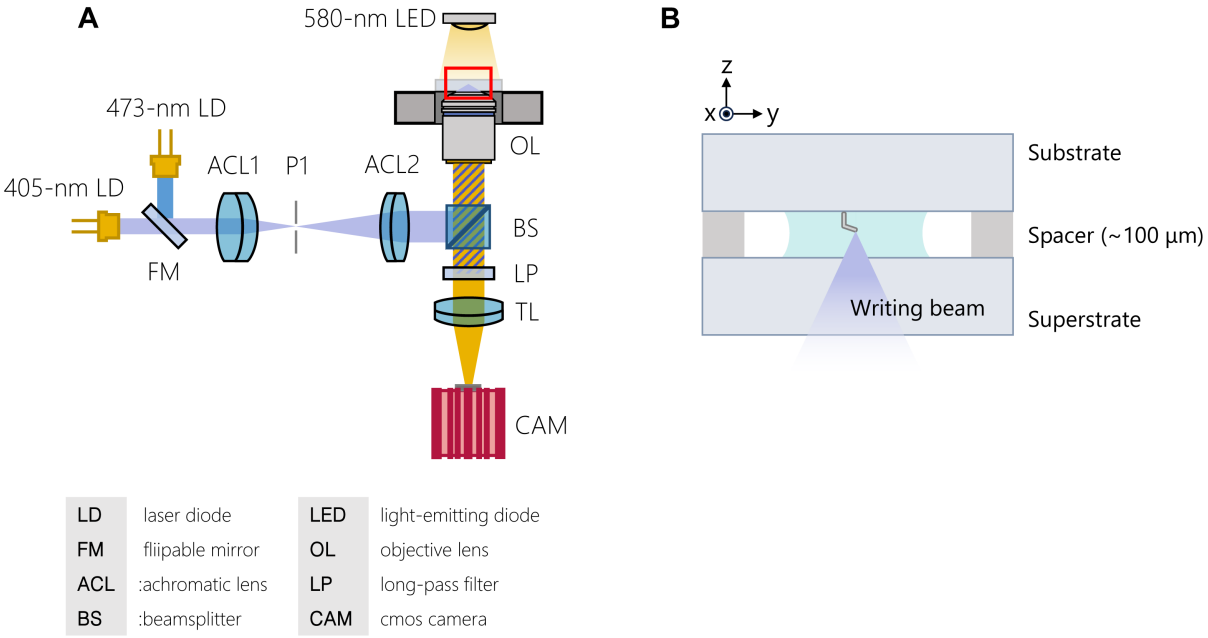

LD	laser diode	LED	light-emitting diode
FM	fliipable mirror	OL	objective lens
ACL	:achromatic lens	LP	long-pass filter
BS	:beamsplitter	CAM	cmos camera

(**A**) Schematics of the homebuilt 3D nanoprinter employed for TPLP. (**B**) Schematic illustration of typical sample configuration used in TPLP.

Supplementary Fig. S3 | Focal intensity distribution of the writing beam

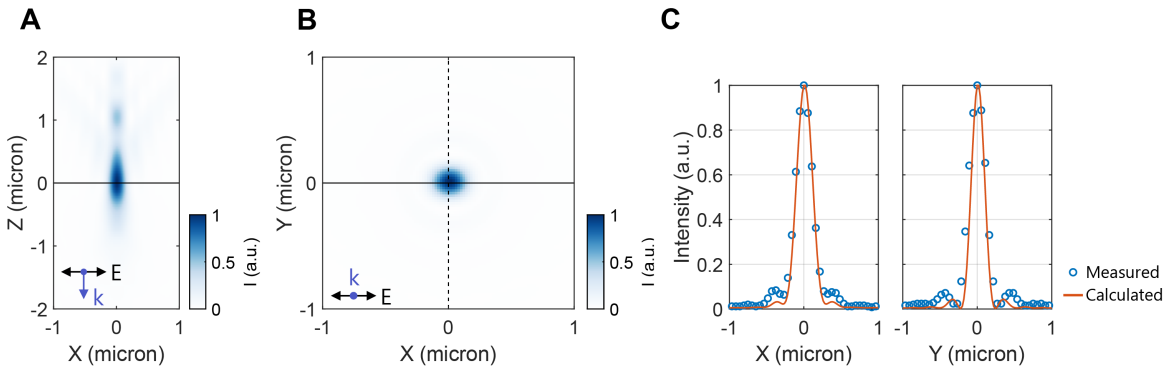

Calculated focal intensity distribution for the experimental configuration used in TPLP. A linearly-polarized beam is tightly focused at the ink-coverslip interface. (**A**) Intensity distribution within the XOZ plane. (**B**) Intensity distribution within the XOY plane. The arrows in (A) and (B) mark the electric field polarizations (black) and the wavevectors (blue). (**C**) Comparisons between the measured intensity profiles and the calculated profiles extracted along the black lines in (B). The full-width at half maximum (FWHM) along X (left) and Y (right) directions of the practical laser focus are evaluated to be 220 nm and 225 nm, respectively. The broadening along with the depolarization imply the presence of residual aberrations.

Supplementary Fig. S4 | Optical responses of nanosized metal particles

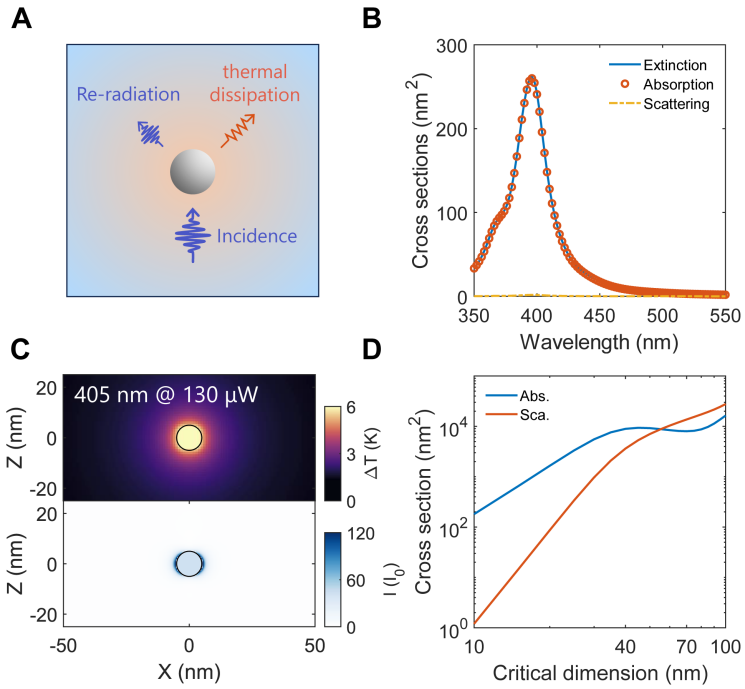

(**A**) Schematic illustration of optical responses of metal nanoparticles (NPs), the incident light is extincted either non-radiatively by absorption, or, radiatively by scattering. The former could induce heating of both the NP and the surroundings, while the latter could lead to reshaped near-field intensity distribution. (**B**) Calculated extinction (blue solid line), absorption (orange dotted line) and scattering (yellow dashed line) spectra of a 10-nm silver NP in the bulk TPLP ink ($n = 1.33$). The particle is illuminated by a broadband planewave incident from $z = +\infty$. (**C**) XOZ slices of simulated relative temperature distribution (upper panel) and optical near-field intensity distribution (lower panel) of a 10-nm silver NP in bulk TPLP ink. The NP is illuminated by a 405-nm monochromatic planewave at an absolute laser power of 130 μW (equivalently, an intensity of 100 kW/cm^2). (**D**) Calculated size-dependent absorption and scattering cross sections of silver NPs at 405 nm.

Supplementary Fig. S5 | Thermal equilibrium timescale in TPLP

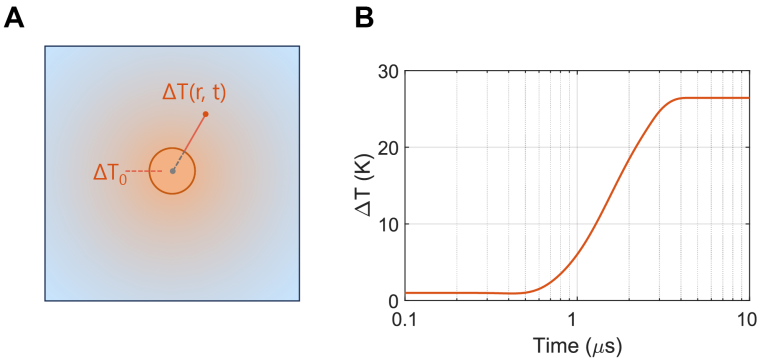

(**A**) Schematic illustration of the typical system involved in TPLP: one source metal NP is heated up by ΔT_0 at $t = 0$ and then held at constant heat-dissipation power for $t > 0$. Thermal equilibrium between the NP and the surroundings causes a temperature rise of $\Delta T(\mathbf{r},t)$ at position $\mathbf{r}$ and time t with respect to the initial temperature. Provided that the inner temperature of a 100-nm NP is brought up by 50 K and then held unchanged, (**B**) the time-dependent temperature variation for a field point located at 100 nm away from the NP surface shows an equilibrium time at around 4 μs.

Supplementary Fig. S6 | Focal temperature distribution without dominating source NPs

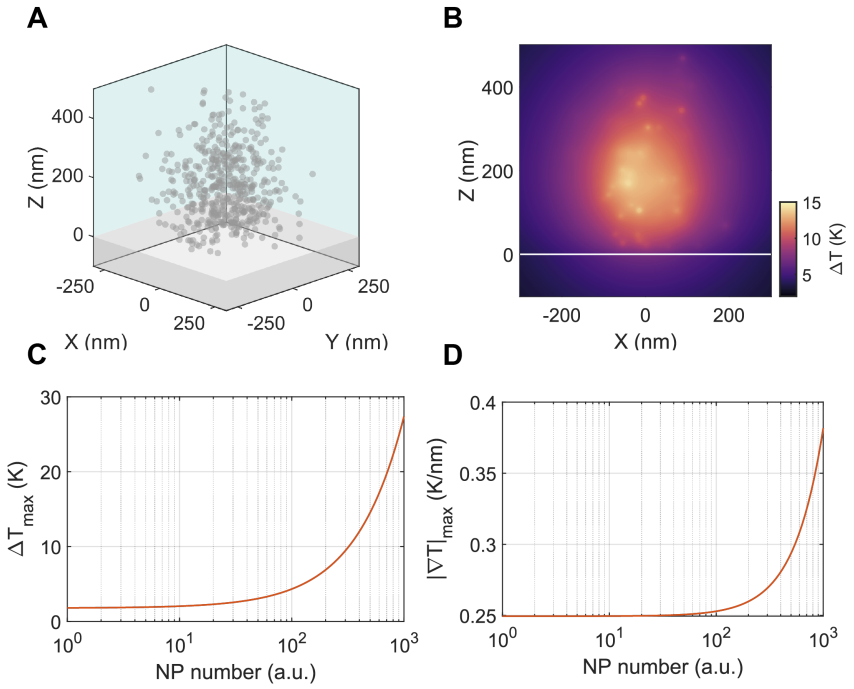

Steady-state temperature distribution in the laser focus, provided the absence of dominating source NP(s). Instead, A cluster of random distributed 10-nm feed NPs is assumed to be illuminated by a 405-nm planewave at an absolute laser power of 130 μW (equivalently, an intensity of 100 kW/cm^2). (**A**) Spatial distribution of the feed NPs in the cluster. The population is set as 512. The NP distribution is presumed to follow random normal distribution, with the standard deviation derived based on the FWHMs of the ideal laser focus., (**B**) XOZ slice of the relative temperature distribution. (**C**) Maximum focal temperature rise as a function of the feed NP population. (**D**) Maximum focal temperature gradient value as a function of feed NP population. Both (C) and (D) show limited local heating and small temperature gradient value (< 1 K/nm) even for a NP population over 500.

Supplementary Fig. S7 | Focal temperature distribution with single dominating source NP

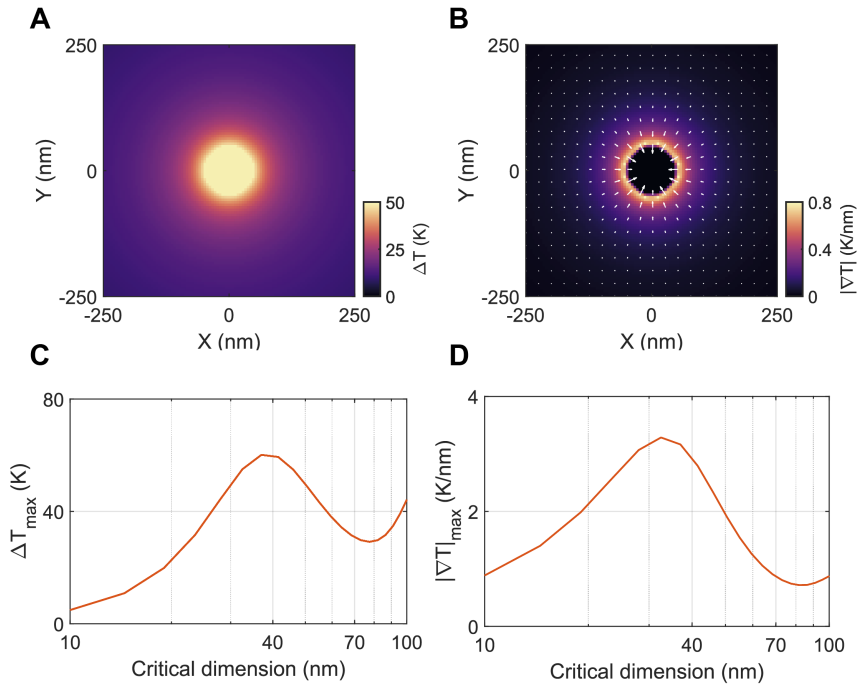

Steady-state temperature distribution in the laser focus, provided the presence of a dominating source NP with a critical dimension of 100 nm. (**A**) XOY slice of the calculated relative focal temperature distribution under the illumination by a 405 nm planewave at an absolute laser power of 130 μW (equivalently, an intensity of 100 kW/cm^2). (**B**) Corresponding temperature gradient distribution of (A), the white arrows indicate the in-plane focal gradient (vectors) at specific field points. (**C**) Maximum focal temperature rise as a function of the critical dimension of the source NP. (**D**) Maximum focal temperature gradient value as a function of the critical dimension of the source NP. Note that contributions from the feed NPs are not taken into account.

Supplementary Fig. S8 | Brownian motion of feed NPs in the heated focus

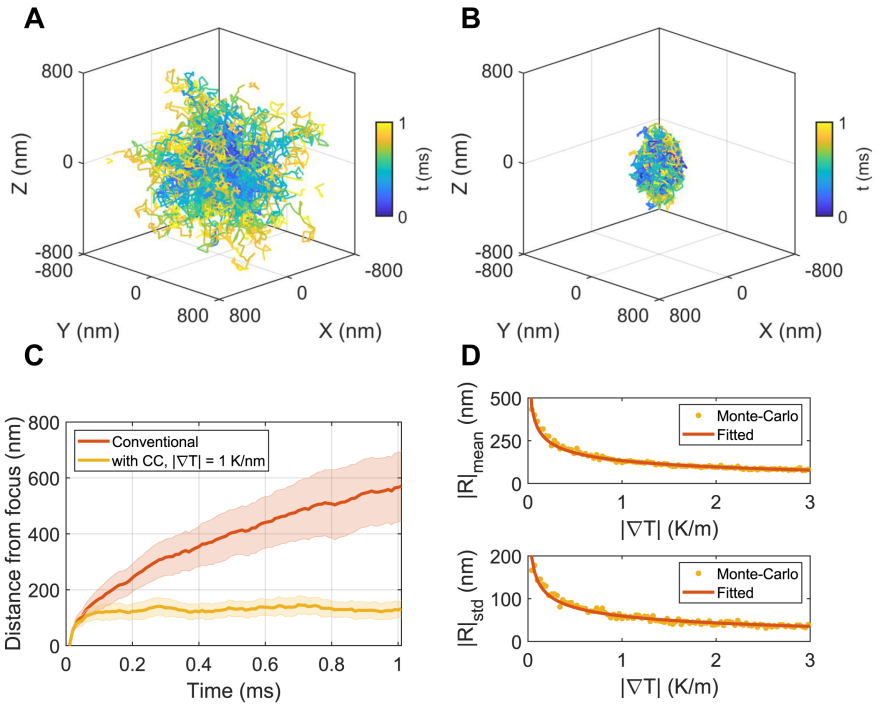

Time-traced trajectories of 100 feed NPs during a time duration Δt of 1 ms are simulated based on Monte-Carolo method, the particles are assumed to be non-interactive with each other and set free at the focal centre at $t = 0$. The absolute temperature at the focal centre is set as 318 K. (**A**) Trajectories of the feed NPs without the presence of confining potentials, homogeneous 3D dispersion of the feed NPs can be observed. (**B**) Trajectories of the feed NPs with the presence of CC potential field, the potential distribution is set according to Eqs. (S35) and (S36), with the potential depth set as $-6k_BT$. The feed NPs are well-confined during the 1-ms period. (**C**) Time-traced average NP displacement from the focal centre for conventional case as (**A**) and TPLP case as (**B**), the shaded areas mark the root mean square displacement at specific time. (**D**) Maximum average displacement (upper panel) and root mean square displacement (lower panel) as functions of the maximum focal temperature gradient values.

Supplementary Fig. S9 | Properties of the Coulombic-confining (CC) field

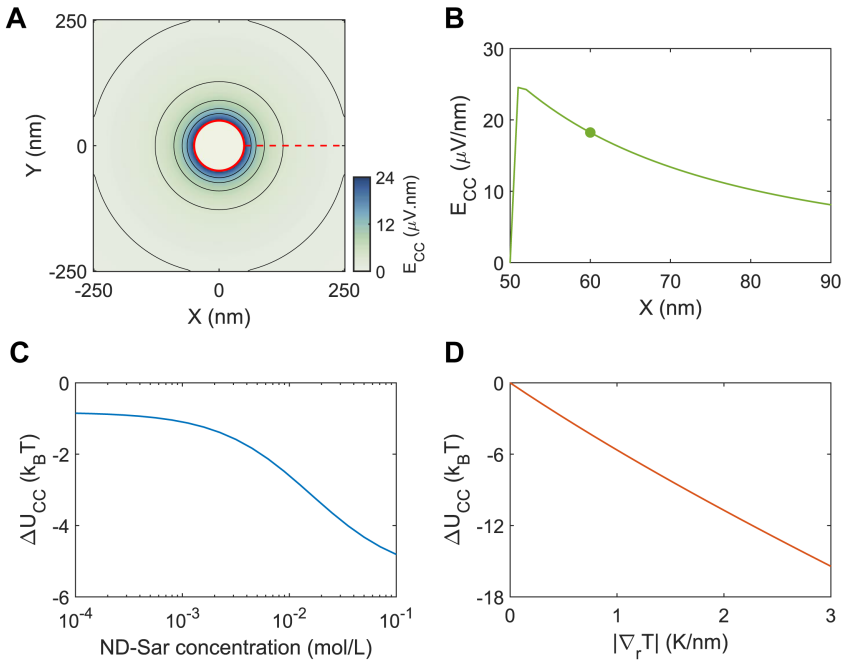

A two-body system, consisted of a 100-nm source NP coupled with a 10-nm feed NP in bulk TPLP ink, is considered. Concentration of ND-Sar and DSAc are set as 0.1 and 0.75 mol/L in accordance with the experimental conditions for 3D TPLP. And, the system is assumed to be heated under illumination of a 405-nm planewave at an absolute laser power of 130 μW (equivalently, an intensity of 100 kW/cm^2). (**A**) XOY slice of the simulated CC field. The red contour marks the NP boundary, while the black contours mark the iso-potential lines. (**B**) Profile of the CC field magnitude, extracted along the red dashed line in (A). The saw-like feature in the plot originates from the insufficient spatial sampling, which leads to failure in resolving of the fast-varying field in about one λ_D from the source NP surface. (**C**) CC potential energy probed by a charged, 10-nm feed NP as a function of ND-Sar concentration. (**D**) CC potential energy probed by the feed NP as a function of the maximum focal temperature gradient value. The CC potential energies in (C) and (D) are evaluated at the green solid dot (i.e., 10 nm away from the source NP surface) marked in (B).

Supplementary Fig. S10 | Feature size statistics of elemental feed NPs in TPLP

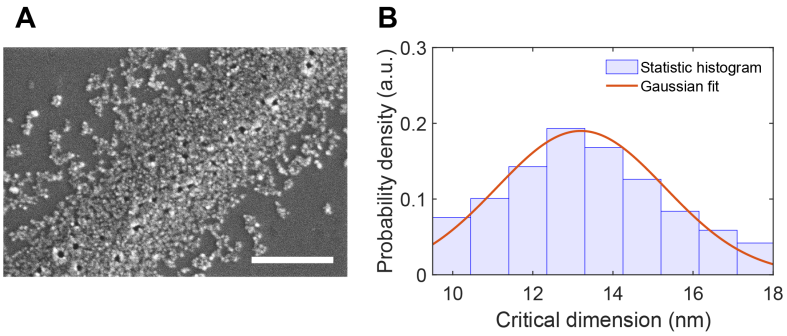

(**A**) High-magnification SEM micrograph of a segment of one of the loosely-packed silver microwires. The micro-wire is printed at 473 nm with the use of a low-NA (0.90) objective, by which means the CC force is weakened due to the small temperature gradient value and allows close inspection of the feed NP morphologies. (**B**) Statistics on the size of 150 randomly-selected feed NPs in (A). The expectation value is measured to be 13.2 nm with a standard deviation of 2.4 nm.

Supplementary Fig. S11 | Properties of the thermo-osmotic potential field

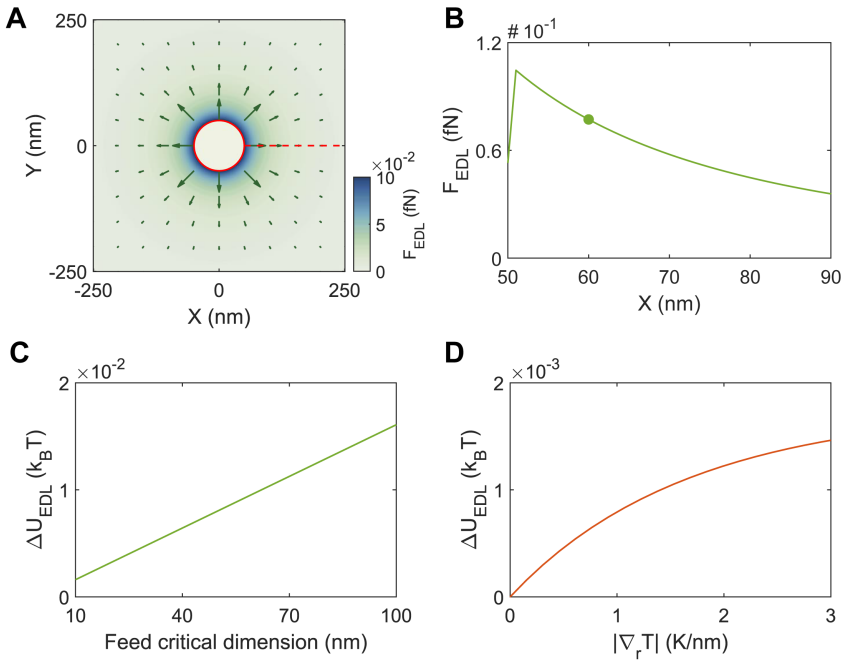

The coupled NP system in Fig.S9 is considered, but with the CC potential field disabled. the system is assumed to be heated under illumination of a 405-nm planewave at an absolute laser power of 130 μW (equivalently, an intensity of 100 kW/cm^2). (**A**) XOY slice of the simulated EDL force map for feed NPs at different field points. The red contour marks the boundary of the source NP and the black arrows indicate the EDL force for feed NPs at specific locations. (**B**) Profile of EDL force magnitude, extracted along the red dashed line in (A). (**C**) Thermo-osmotic potential energy as a function of the critical dimension of the feed NP probe (the surface potential of which is set as constant). (**D**) Thermo-osmotic potential energy probed by a 10-nm feed NP as a function of the maximum focal temperature gradient value. The thermo-osmotic potential energies variations in (C) and (D) are evaluated at the green solid dot (i.e., 10 nm away from the source NP surface) marked in (B).

Supplementary Fig. S12 | Exclusion of optical trapping effect in TPLP

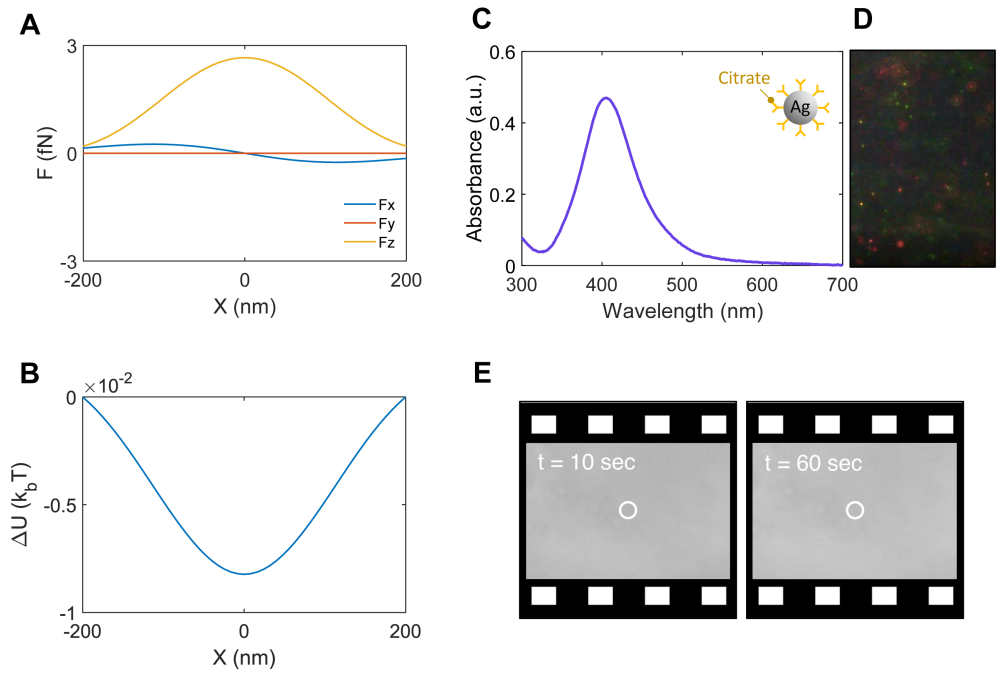

For optical force, a 10-nm feed NP is assumed to be free to move in the laser focus, with all heat-driven NP transport effects disabled. The absolute laser power is set at 200 μW. (**A**) Total optical force components as a function of NP position. The focal centre is set as the origin. (**B**) Computed potential energy contributed from the attractive gradient force (X and Y components) (**C**) Measured UV-Vis absorption spectrum of a commercially-available citrate-capped silver NP (D = 25 nm) suspension, 30-times diluted. (**D**) Snapshot of dark-field micrograph of the diluted silver NP suspension employed for optical trapping test. (**E**) In-situ snapshots during trapping test at 10 seconds (left) and 60 seconds (right) after turning on the laser. The 405-nm laser (660 μW) is focused at the water-coverslip interface and the focus location is marked by the white circle (the laser spot cannot be seen due to the presence of laser-line filter before the CMOS camera).

Supplementary Fig. S13 | Optical near-field of coupled source-feed NPs in TPLP

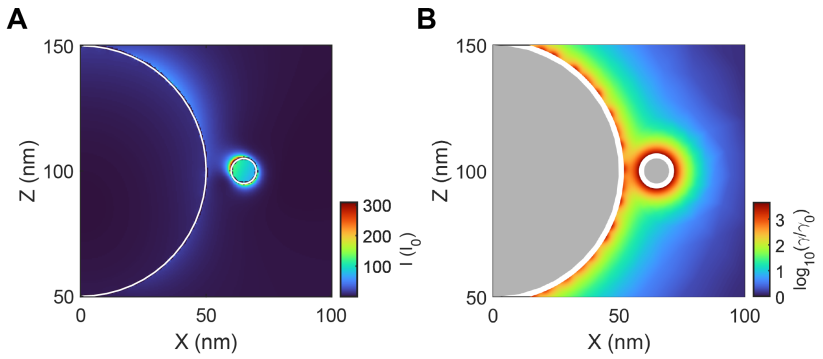

Again, the coupled NP system is considered. The surface-to-surface distance between the two NPs is set as 10 nm to activate near-field enhancement by gap surface-plasmon resonance. (**A**) XOZ slice of calculated near-field intensity distribution upon illumination by a 405-nm monochromatic planewave, the electric field polarization is directed along the X axis. (**B**) False-color map of photoreduction rate for a probe dipole with transition energy of 3.06 eV, attained by consecutively placing the dipole at the field points in (A), during which the absorption rate at each location is recorded and normalized to the free-space value.

Supplementary Fig. S14 | Linewidth of nanowires printed with and without heat transduction

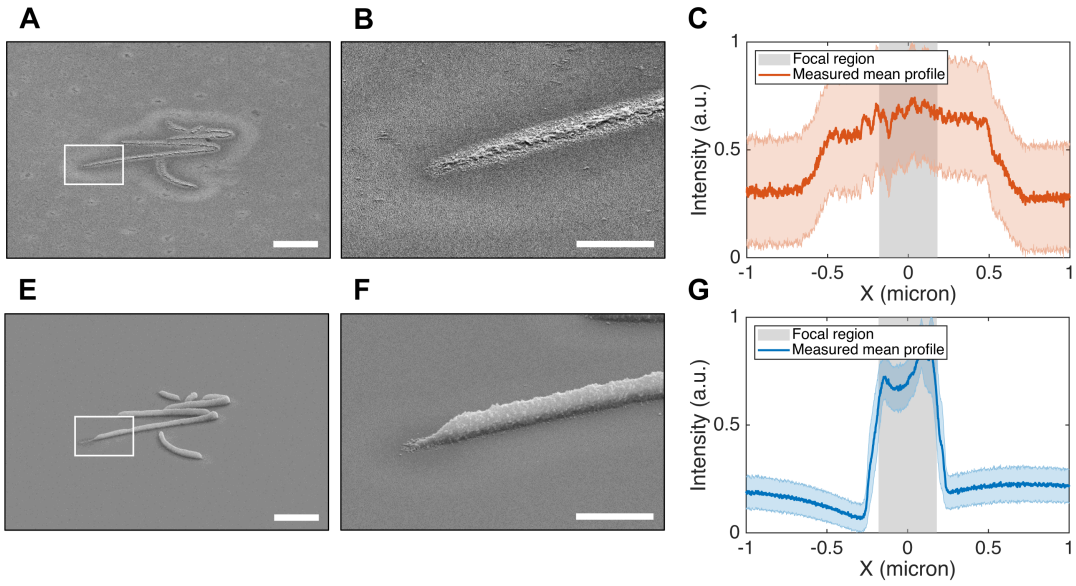

(**A**) Tilted SEM micrograph of the Chinese character 'light' shown in Fig. 2d. (**B**) Zoomed view of the rectangular area marked in (A). (**C**) Normalized secondary electron intensity from the wire elements in the (A), evaluated from the SEM micrograph and averaged over the whole pattern. The shaded orange area marks the standard deviation of the intensity, the gray area marks the focal region and spans the FWHM of the ideal laser focus. (**E**) Tilted SEM micrograph of the Chinese character 'light' shown in Fig. 2i. (**F**) Zoomed view of the rectangular area marked in (E). (**G**) Normalized secondary electron intensity from the wire elements in the (F), evaluated from the SEM micrograph and averaged over the whole pattern. The shaded blue area marks the standard deviation of the intensity, the gray area marks the focal region and spans the FWHM of the ideal laser focus. Scale bars: (A) and (E), 5 μm; (B) and (F), 2 μm.

Supplementary Fig. S15 | Position and temperature dependent exposure dose accumulation in TPLP

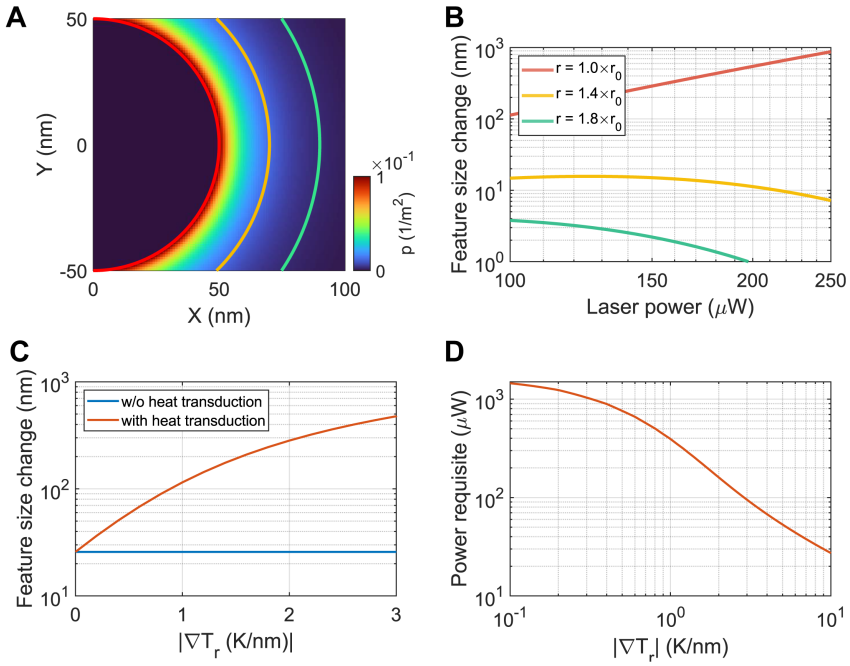

The establishment of the CC potential field could introduce extra nonlinear optical response to the overall photoreaction. (**A**) Zoom-in view of the CC-potential reshaped probability density distribution that is demonstrated in Fig.2G. (**B**) Simulated feature size changes on a primitive source NP structure as functions of laser power, extracted on the contour marked in (A). (**C**) Simulated feature size changes on a primitive source NP structure as functions of the maximum radial temperature gradient value in the focus, the absolute laser power is fixed at 130 μW (equivalently, an intensity of 100 kW/cm^2). The introduction of heat transduction (orange curve) leads to nonlinearly increased exposure dose, which is in sharp contrast with the constant value for the case without heat transduction. (**D**) Simulated power requisite for reaching threshold exposure dose as a function of the maximum focal temperature gradient value. Decreae on power requisite by one order of magnitude is predicted provided that additional temperature gradient modulations are designed and introduced to further increase the focal temperature gradient value during printing.

Supplementary Fig. S16 | Plasmonic laser colour printing by metallic exposure dose control

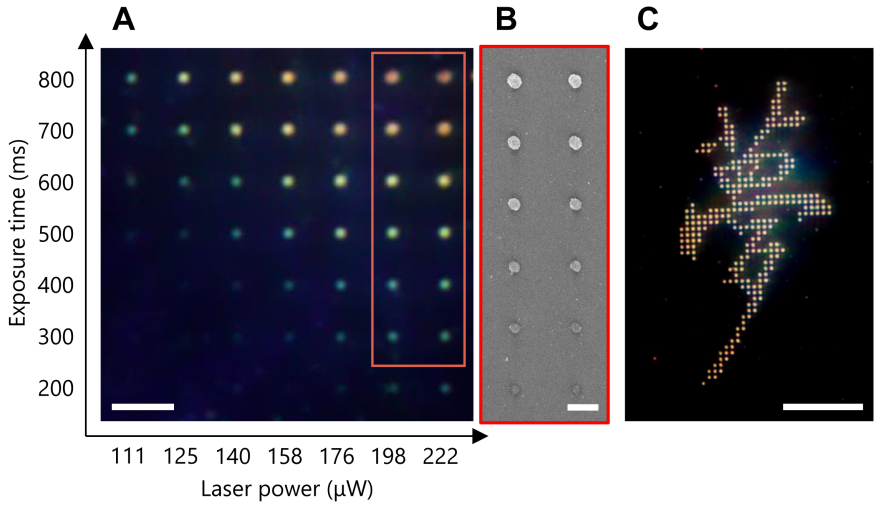

(**A**) Dark-field optical micrograph of a printed silver nanodot array, from which the elements with representative plasmonic colours are elected and displayed in Fig. 3a. (**B**) SEM image of the elements enclosed in the red rectangle in (A). (**C**) A pixelated pattern of the Chinese character 'dream', the exposure dose is fixed at 140 μW @ 800 ms. The pixel pitch is 1.5 μm. Scale bar: (A), 3 μm; (B), 1 μm; (C), 20 μm.

Supplementary Fig. S17 | Extended data about micromirrors printed by TPLP

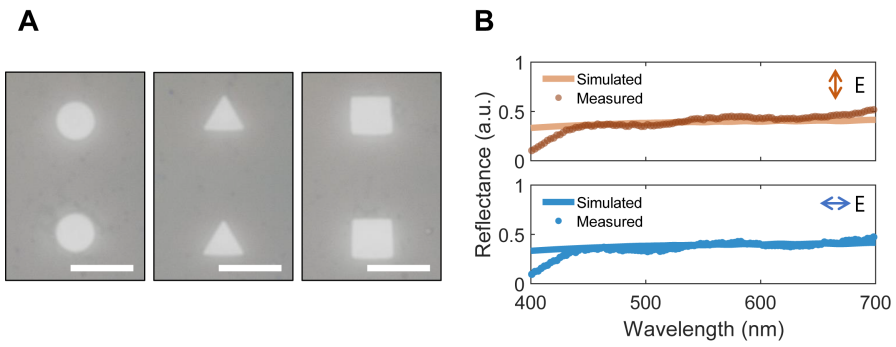

(**A**) Bright-field optical micrographs of as-printed micromirrors in three different shapes. Scale bar: 10 μm. (**B**) Comparisons between measured (dotted curve) and simulated (solid curve) polarized reflection spectra of the micromirrors, the spectral data are averaged from the mirrors presented in (A).

Supplementary Fig. S18 | Electrical properties of the elemental nanowires in TPLP

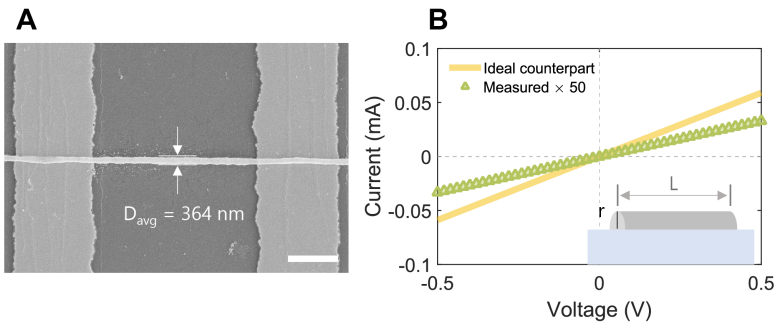

(**A**) SEM micrograph of one representative silver nanowire printed on gold interdigital electrodes. Scale bar: 3 μm. (**B**) Measured U-I curve of the nanowire (line with triangle marks, averaged from three wires) and expected curve of an ideal counterpart made of pure silver (yellow solid line).

Supplementary Fig. S19 | Extended data about the 3D conductive network structures

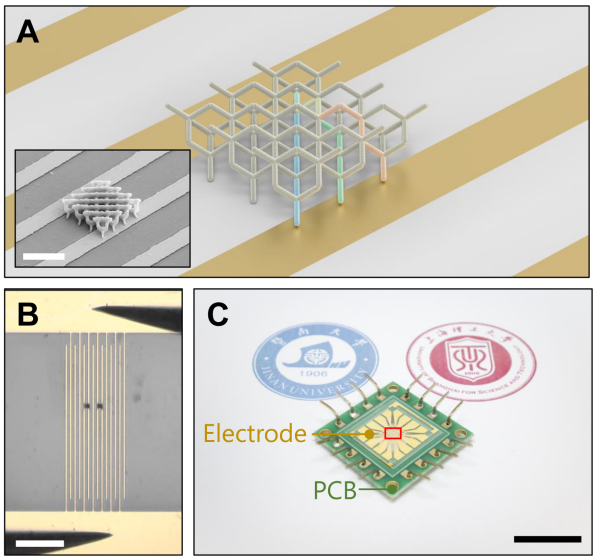

(**A**) Schematics of a 3D silver network structure on gold interdigital electrodes, the colored rods mark the three of the possible 3D conducting routes during linear voltammetry measurements. Inset: zoomed SEM micrograph of the TPLP-printed structure. (**B**) In-situ BF optical micrograph of the test region during two-probe measurements. (**C**) Photograph showing the packaged sample on a circuit board. Scale bars: inset in (A), 10 μm; (B), 200 μm; (C) 20 mm.

Supplementary Fig. S20 | Extended 3D structure gallery

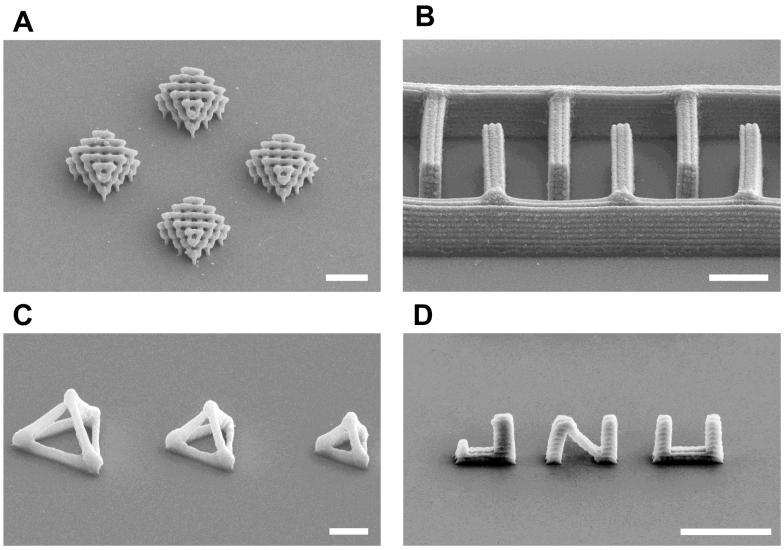

(**A**) Arrayed diamond-structured silver lattices, the lattice constant is fixed at 1.3 μm. (**B**) A wall structure printed by layer-wise stacking. (**C**) An array of triangular cone structures, the side lengths are 4 μm (left), 3 μm (middle), and 2 μm (right). (**D**) Standing letters 'JNU' printed by layer-wise stacking. Scale bars: (A), (B) and (D), 5 μm; (C), 2 μm. Tilt angles: (A), 45 degrees, (B-D), 60 degrees.

Supplementary Table S1 | Summary on recipes of TPLP inks used in this work.

Recipes	Precursor[a]	Capping agents[a]	Reducing agents[b]	Purposes
R1	DSAc (0.25 mol/L)	ND-Sar (0.10 mol/L)	TPETA (0.50 wt%)	For 2D TPLP experiments
R2	DSAc (0.75 mol/L)	ND-Sar (0.10 mol/L)	TPETA (1.25 wt%)	For 3D TPLP experiments
R3	DSAc (0.25 mol/L)	Sodium citrate (0.10 mol/L)	TPETA (1.25 wt%)	For control experiment shown in Fig. 2c-e

Note:
[a]: molar concentration in the final blend
[b]: mass concentration in the final blend

Supplementary Table S2 | Summary on exposure dose parameters used for the main-text figures.

Figures	Structure type	Laser power	Scanning velocity (exposure time)
Figure 2c, 2h	0D nanodot structures	ca. 150 μW	400 ms
Figure 2d, 2i	2D curvilinear structures	ca. 230 μW	4 μm/s
Figure 2m	0D nanodot structure	ca.120~220 μW	400 ms
Figure 2n	0D nanodot structure	ca. 130 μW	200~800 ms
Figure 3a, 3b	0D nanodot structure 2D pixelated pattern	ca. 110~220 μW	800 ms
Figure 3c	2D planar structure	ca. 160 μW	1 μm/s
Figure 3e	2.5D structure	ca. 210 μW	4 μm/s
Figure 4a, 4f	3D lattice structures	ca. 230 μW	4 μm/s
Figure 4h	3D topological structures	ca. 180 μW	2 μm/s

Supplementary Table S3 | Summary on optical diffraction limits in TPLP

Directions	Absolute value (nm)	Relative value (λ)
X	324	0.82
Y	446	1.14
Z	956	2.36

Note:
Derived based on the nominal optical parameters, without inclusion of residual aberrations in the optical system. Laser wavelength, 405 nm; incident electric-field polarization: x-linearly polarized; NA, 1.20; index of immersion medium: 1.33

Supplementary Table S4 | Summary on optical sources required by different 3D metal printing techniques

Quantities	Descriptions	Typical (peak) power requisite[a]	Typical Footprint[b]	Typical apparatus cost[b]
Ultrafast lasers	Commonly used for multiphoton-absorption based techniques	10^2~10^5 W	10^7~10^8 mm^3	USD 10^4~10^5 (CNY 10^5~10^6)
High-power CW lasers	Commonly used for laser powder-fusion based techniques	10^0~10^2 W	10^7~10^8 mm^3	USD 10^5 (CNY 10^6)
Diode laser	Laser source required for implementation of TPLP	~10^{-4} W	10^2 m~$10^6$$mm^3$	USD 10^1~10^3 (CNY 10^2~10^3)

Note:

a) Power requisite refers to the minimum source power output to support 3D printing in different methods, power loss caused by optical elements in the optical system are not included.

b) Variation on costs and footprints usually relate to the specification of the package type, operating wavelength and the maximum power output.

Supplementary Movies.

Movie S1.
Movie of typical 2D printing experiment with TPLP configuration (with R1 in supplementary table S1). Exposure condition: 230 μW @ 4 μm/s. The movie is 2-times speeded up.

Movie S2.
Movie of typical 2D printing experiment with control group configuration (with R3 in supplementary table S1). Exposure condition: 230 μW @ 4 μm/s. The movie is 2-times speeded up.

Movie S3.
Movie of typical 3D printing experiment with TPLP configuration (with R2 in supplementary table S1). Exposure condition: 230 μW @ 4 μm/s. The movie is 3-times speeded up.

Movie S4.
Movie of optical trapping test using the same 3D nanoprinter for TPLP, with the focus area marked by the white circle. Exposure condition: 660 μW. The movie is 3-times speed-up.

Supplementary references

43. Walker, S. B. & Lewis, J. A. Reactive Silver Inks for Patterning High-Conductivity Features at Mild Temperatures. *Journal of the American Chemical Society* **134**, 1419-1421, doi:10.1021/ja209267c (2012).

44. Lin, J., Rodríguez-Herrera, O. G., Kenny, F., Lara, D. & Dainty, J. C. Fast vectorial calculation of the volumetric focused field distribution by using a three-dimensional Fourier transform. *Opt. Express* **20**, 1060-1069, doi:10.1364/OE.20.001060 (2012).

45. García de Abajo, F. J. & Howie, A. Retarded field calculation of electron energy loss in inhomogeneous dielectrics. *Physical Review B* **65**, 115418, doi:10.1103/PhysRevB.65.115418 (2002).

46. Blanco, L. A. & García de Abajo, F. J. Spontaneous light emission in complex nanostructures. *Physical Review B* **69**, 205414, doi:10.1103/PhysRevB.69.205414 (2004).

47. Giannini, V., Fernández-Domínguez, A. I., Heck, S. C. & Maier, S. A. Plasmonic Nanoantennas: Fundamentals and Their Use in Controlling the Radiative Properties of Nanoemitters. *Chemical Reviews* **111**, 3888-3912, doi:10.1021/cr1002672 (2011).

48. Novotny, L. & Hecht, B. Principles of nano-optics. (Cambridge university press, 2012).

49. Linic, S., Aslam, U., Boerigter, C. & Morabito, M. Photochemical transformations on plasmonic metal nanoparticles. *Nature Materials* **14**, 567-576, doi:10.1038/nmat4281 (2015).

50. Cortés, E., Xie, W., Cambiasso, J., Jermyn, A. S., Sundararaman, R., Narang, P., Schlücker, S. & Maier, S. A. Plasmonic hot electron transport drives nano-localized chemistry. *Nature Communications* **8**, 14880, doi:10.1038/ncomms14880 (2017).

51. López-García, J. J., Aranda-Rascón, M. J. & Horno, J. Electrical double layer around a spherical colloid particle: The excluded volume effect. *Journal of Colloid and Interface Science* **316**, 196-201, doi:https://doi.org/10.1016/j.jcis.2007.07.054 (2007).

52. Hedberg, J., Lundin, M., Lowe, T., Blomberg, E., Wold, S. & Wallinder, I. O. Interactions between surfactants and silver nanoparticles of varying charge. *Journal of Colloid and Interface Science* **369**, 193-201, doi:https://doi.org/10.1016/j.jcis.2011.12.004 (2012).

53. Badawy, A. M. E., Luxton, T. P., Silva, R. G., Scheckel, K. G., Suidan, M. T. & Tolaymat, T. M. Impact of Environmental Conditions (pH, Ionic Strength, and Electrolyte Type) on the Surface Charge and Aggregation of Silver Nanoparticles Suspensions. *Environmental Science & Technology* **44**, 1260-1266, doi:10.1021/es902240k (2010).